J|A|C|S
JOURNAL OF THE AMERICAN CHEMICAL SOCIETY
Article
pubs.acs.org/JACS

# Liquid-Phase Syntheses and Material Properties of Two-Dimensional Nanocrystals of Rare Earth−Selenium Compound Containing Planar Se Layers: $RESe_2$ Nanosheets and $RE_4O_4Se_3$ Nanoplates

Jun Gu,[‡] Ze-Qiong Zhao,[‡] Yi Ding,[†] Hong-Liang Chen, Ya-Wen Zhang,* and Chun-Hua Yan*

Beijing National Laboratory for Molecular Science, State Key Laboratory of Rare Earth Materials and Applications, PKU-HKU Joint Laboratory in Rare Earth Materials and Bioinorganic Chemistry, College of Chemistry and Molecular Engineering, Peking University, Beijing 100871, China

*Supporting Information*

**ABSTRACT:** Synthesis of diverse two-dimensional nanostructures with unique material properties is of current interest and multidisciplinary importance but remains a challenge for trivalent rare earth (RE)−selenium (Se) compounds because of the weak affinity between hard rare earth cations and soft selenium anions. In this article, for the first time, we report a mild solution approach toward a series of two-dimensional trivalent RE−selenium compound nanocrystals, namely $RESe_2$ nanosheets (RE = La to Nd, for $EuSe_2$, nanobars were obtained) and $RE_4O_4Se_3$ nanoplates (RE = Nd, Sm, Gd to Ho), under a high chemical potential of selenium obtained by activating $SeO_2$ powder with oleylamine in high boiling point organic solvents. Both kinds of nanocrystals contain Se with −1 valence in planar Se layers, allowing for a great variability in their crystal structures. Satellite diffraction peaks were observed in the electron diffraction pattern of $LaSe_2$ nanosheets, indicating the presence of Peierls distortion in the Se layers. In the $RE_4O_4Se_3$ nanoplates, the interaction between $Se^{2-}$ ions and $[Se-Se]^{2-}$ dumbbells in the Se layers increases when the radii of the $RE^{3+}$ ions decrease along the lanthanide series, resulting in a narrower optical band gap (from 1.96 to 1.73 eV). The $LaSe_2$ nanosheet films fabricated by drop-casting exhibited good electrical conductivity at room temperature (about 1 Ω·$cm^{-1}$). Further, the $RE_4O_4Se_3$ nanoplates showed very high light extinction capacity in the visible region (extinction coefficient $\mu_i$: $4.4 \times 10^5$ $cm^{-1}$ for $Nd_4O_4Se_3$, and $3.1 \times 10^5$ $cm^{-1}$ for $Gd_4O_4Se_3$), comparable to that ($5 \times 10^5$ $cm^{-1}$) of $CuInS_2$ commonly used in solar cells.

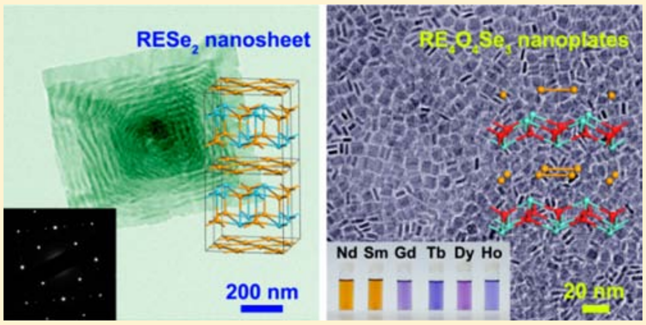

## ■ INTRODUCTION

Colloidal methods have been used to synthesize numerous two-dimensional (2D) nanocrystals (NCs).[1,2] Chalcogenide (sulfide, selenide, and telluride) compounds with layered structures, such as topological insulators,[3] ferromagnets,[4] charge density wave conductors,[5−7] and superconductors,[8] are one family of the most important 2D materials. They demonstrate practical applications including transistors,[9,10] supercapacitors,[11] and thermoelectric devices,[12] etc. Compared with micromechanical exfoliation[9] and vapor deposition,[10] colloidal methods promise highly efficient preparation of free-standing 2D chalcogenide nanomaterials at lower cost.[13−21] For example, Hyeon and co-workers synthesized CdSe nanoribbons with uniform thickness of 1.4 nm through a Lewis acid−base reaction between cadmium cations and selenocarbomate anions at low temperature.[13] Dubertret and co-workers realized the thickness controlled synthesis of CdSe platelets.[14] Weller and co-workers showed that single-crystal ultrathin PbS nanosheets could be synthesized by oriented attachment of smaller PbS nanocubes, and the as-formed nanosheets could be further integrated into a photodetector device through a simple spin-coating method.[17] Additionally, colloidal 2D nanomaterials, including chalcogenides of d-block elements,[15,16,19] $In_2S_3$,[20] SnSe,[21] have been synthesized.

Among chalcogenides and oxy-chalcogenides of various metals, those of rare earth (RE) elements possess interesting structures and properties. Doert and co-workers explored a series of RE polychalcogenide crystals prepared by chemical transport reaction of elementary substances, containing infinite planar layers of chalcogen atoms, with the chemical formulas as $REX_2$,[22] REXY,[23] $REX_{2-\delta}$[24,25] and $REXY_2$[26,27] (X, Y = S, Se, Te). Many of these materials were described to be 2D charge density wave compounds. Due to the special electronic structure, the chalcogen layers in the crystals adopt Peierls distortion, resulting in satellite reflections in diffraction characterization. RE oxy-selenide with the formula of $RE_4O_4Se_3$ is another type of material containing Se-planes with parallel $-Se^{2-}-[Se-Se]^{2-}-$ chains. Schleid and co-workers prepared $RE_4O_4Se_3$ (RE = La to Nd, Sm) through the solid-state reactions of RE metal, elemental selenium and $SeO_2$, and investigated their optical and magnetic proper-

**Received:** March 21, 2013
**Published:** May 15, 2013

dx.doi.org/10.1021/ja4028583 | *J. Am. Chem. Soc.* 2013, 135, 8363−8371

ties.[28,29] It is of great interest to examine the properties of these materials when the thickness of the crystal is confined within several nanometers.

In recent years, a lot of efforts have been devoted to the syntheses of colloidal NCs of different types of compounds of trivalent RE, including oxide ($RE_2O_3$),[30,31] fluoride ($REF_3$),[32,33] $NaREF_4$,[34,35] oxy-halide (REOX, X = F, Cl),[36,37] and oxysulfide ($RE_2O_2S$).[38−41] Among these materials, RE oxide, fluoride, and oxysulfide NCs exhibit 2D disk morphology. According to hard soft acid base (HSAB) theory,[42] trivalent RE ions are classified as hard acid, possessing strong affinity toward oxygen and halide ions but weak affinity toward $S^{2-}$, $Se^{2-}$, and $Te^{2-}$ ions. The syntheses of EuS,[43] EuSe,[44] and $EuSe_2$[45] NCs have been reported previously, but in all of these materials Eu element is divalent. In our previous work, by introducing alkali metal ions (e.g., $Na^+$) as mediator and dopant, doped $RE_2O_2S$ nanoplates[39,40] and $NaRES_2$ NCs[46] were prepared. So far, the synthesis of trivalent RE selenide and oxy-selenide NCs has still remained a big challenge in this field.

In this work, for the first time, two types of 2D NCs, $RESe_2$ nanosheets (RE = La to Nd, for $EuSe_2$, nanobars were obtained) and $RE_4O_4Se_3$ nanoplates (RE = Nd, Sm, Gd to Ho), were synthesized in a mixture of oleic acid, oleylamine, and 1-octadecene. Excess $SeO_2$ was used as Se source and activated by oleylamine to provide high chemical potential of Se element in the reaction mixture. The formation conditions of these two types of NCs are discussed. Among these NCs, $LaSe_2$ nanosheets with side length of about 1 μm were generated from screw dislocation driven growth. Satellite diffraction peaks were observed in the electron diffraction pattern of $LaSe_2$ nanosheets, indicating the distortion of the Se layers. Furthermore, $LaSe_2$ nanosheet films fabricated with a spin-coating method exhibited good electrical conductivity at room temperature. $RE_4O_4Se_3$ nanoplates displayed high light-extinction property in visible light region, which might endow them with promising applications in light filters and solar cells. The optical band gap of $RE_4O_4Se_3$ nanoplates decreased from light RE to heavy RE, possibly due to the interaction between $Se^{2-}$ ions and $[Se-Se]^{2-}$ dumbbells caused by lattice shrinkage.

## ■ EXPERIMENTAL SECTION

**Materials.** Oleic acid (OA; 90%, Aldrich), oleylamine (OM; > 80%, Acros), 1-octadecene (ODE; > 90%, Acros), cerium(III) acetate hydrate ($Ce(Ac)_3 \cdot xH_2O$; 99.9% metals basis, Aldrich), RE oxides ($RE_2O_3$, RE = La, Pr, Nd, Sm to Ho; > 99.99%), acetylacetone (Hacac; A. R. grade), selenium dioxide ($SeO_2$, A. R. grade), trioctylphosphine (TOP; 90%, Aldrich), nitric acid ($HNO_3$; A. R. grade), ammonia ($NH_3 \cdot H_2O$; A. R. grade), sodium hydroxide (NaOH; > 96%), absolute ethanol (>99.7%), and cyclohexane (>99.5%) were used as received.

**Synthesis of $RESe_2$ (RE = La to Nd, Eu) and $RE_4O_4Se_3$ (RE = Nd, Sm, Gd to Ho) NCs.** RE acetylacetonate ($RE(acac)_3$, RE = La, Pr, Nd, Sm to Ho) was prepared by following the previously reported procedure.[31] The reaction parameters for every sample were listed in Table S1. Schlenk line was used under $N_2$ atmosphere. $RE(acac)_3$ or $Ce(Ac)_3$ (0.5 mmol), $SeO_2$, OA (1.41 g), OM (4.55 g), and ODE (5.05 g) were loaded into a three-neck flask (100 mL) on a heater with a magnetic stirrer at room temperature. The mixture was heated under vacuum and kept at 80 °C for 5 min and at 100 °C for 20 min, to remove water and oxygen and to form RE oleate in situ.[46] The mixture was then heated to the synthetic temperature listed in Table S1 at a rate of 20 °C·min$^{-1}$ and kept at this temperature for a certain duration (as listed in Table S1) under $N_2$. Then the mixture was air cooled to 160 °C, and TOP (0.7 mL when 0.222 g of $SeO_2$ was added, 1.5 mL when 0.444 g of $SeO_2$ was added) was injected into the flask to reduce elemental Se byproduct. The mixture was kept at 120 °C for 5 min and then was cooled to room temperature, and 40 mL ethanol was added, followed by centrifugation at 7800 rpm for 10 min. The supernatant was discarded, and the precipitate was dispersed in 10 mL cyclohexane under ultrasonic wave. After centrifugation at 3000 rpm for 3 min, the black or dark brown precipitate A and the supernatant B were separated by decantation.

To purify $RESe_2$ NCs, the precipitate A should be washed by cyclohexane for three times. For each time, the precipitate was dispersed in 10 mL cyclohexane, and the mixture was treated under ultrasonic wave for 5 min, followed by centrifugation at 3000 rpm for 3 min. Then the supernatant was discarded. Finally, the precipitate was dried in vacuum or redispersed in cyclohexane for further characterization.

To obtain $RE_4O_4Se_3$ nanoplates, 20 mL of ethanol was added into the supernatant B, followed by centrifugation at 18 000 rpm for 10 min. The supernatant was discarded, and the precipitate was redispersed in 10 mL of cyclohexane. The same procedure was conducted once again. At last, the nanoplates could be preserved in cyclohexane or as powder sample after vacuum drying.

**Resistivity Measurement of $LaSe_2$ Nanosheet Films.** The $LaSe_2$ films for electrical measurements were prepared by drop-casting 150 μL of the dispersion of as-synthesized $LaSe_2$ nanosheets (10 mg·mL$^{-1}$) onto silicon wafers (1 × 1 cm) covered with 300 nm thick thermally grown octadecyltrichlorosilane-modified silicon dioxide surface. Then the thickness of the film was about 2 μm. The as-deposited samples were dried at 80 °C for 30 min, followed by thermal treatment at 300 °C in air for 30 min. Four-electrode configuration was used to minimize the contact resistance. Thermal evaporation was used to deposit metal electrodes, with chromium/gold (5 nm/50 nm) through a shadow mask. The channel length and width were 700 μm and 4 mm, respectively. Resistivity measurements of as-prepared films were carried out on a CHI 840B electrochemical analyzer (CH Instrument, TX, U.S.A.). Constant current was loaded on the outer two electrodes, and the voltage between the inner two electrodes was measured.

**Instrumentation.** X-ray diffraction (XRD) patterns of the dry powders were characterized on a Rigaku D/MAX-2000 diffractometer (Japan) with a slit of 1/2° at a scanning speed of 2°·min$^{-1}$ using Cu Kα radiation. Samples for transmission electron microscopy (TEM) analysis were prepared by drying a drop of cyclohexane dispersion of the NCs on copper grids coated by amorphous carbon. TEM, selected area electron diffraction (SAED), high-resolution TEM (HRTEM), and energy dispersive X-ray spectroscopy (EDS) analyses were performed on a FEG-TEM (JEM-2100F, JEOL, Japan) operated at 200 kV. Particle sizes were counted from at least 50 NCs. Samples for scanning electron microscopy (SEM) and atomic force microscopy (AFM) analyses were prepared by drying a drop of diluted cyclohexane dispersion of NCs on silicon wafers. SEM analyses were conducted on a FEG-SEM (S-4800, Hitachi, Japan) operated at 8.0 kV. The AFM images were acquired with Nanoscope IIIA multimode AFM (Digital Instruments) using tapping mode at room temperature. The absorption spectra were taken on a UV−vis spectrophotometer (UV-3100, Shimadzu, Japan). Quartz absorption cells with optical length of 1 cm were used. Infrared (IR) spectra were taken on a Bruker Vector22 FTIR spectrometer (Germany). The concentrations of the NCs in the dispersions were determined by inductively coupled plasma atomic emission spectrometer (ICP-AES, PROFILE SPEC, Leeman, U.S.A.). To prepare the solution for ICP-AES analysis, 1.000 mL of NCs dispersion in a crucible was first dried on a vapor bath. Then the crucible was put into a muffle furnace and kept at 800 °C for 3 h. After the crucible cooled down, the residue was dissolved by concentrated nitric acid and transferred to a volumetric flask. C−H−N elemental analysis was conducted on a vario EL elemental analyzer (Elementar Analysensysteme GmbH, Germany). X-ray photoelectron spectroscopy (XPS) analysis was taken on an Axis Ultra imaging photoelectron spectrometer (Kratos Analytical Ltd., U.K.).

## RESULTS AND DISCUSSION

**Structure Characterizations of $RESe_2$ Nanosheets.** (RE = La to Nd, Eu) NCs could be prepared with the method presented in the Experimental Section. Among them, $RESe_2$ (RE = La to Nd) nanosheets appeared as black powder, while $EuSe_2$ nanobars were brown powder. When the black powder of $LaSe_2$ nanosheets was compressed, metallic luster could be observed on the surface of the sample, indicating that $LaSe_2$ nanosheets may possess high conductivity. A detailed structure characterization of the $LaSe_2$ nanosheets is shown in Figure 1.

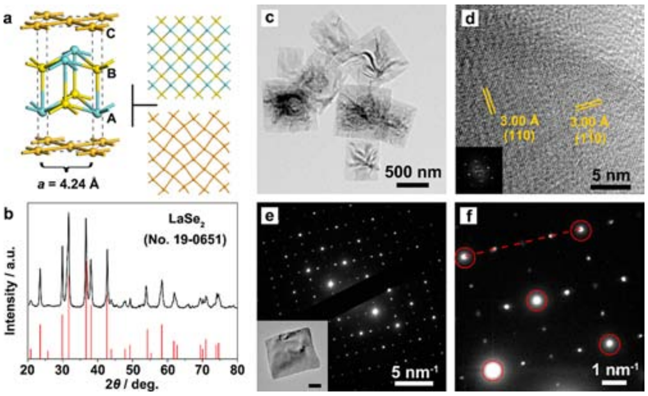

**Figure 1.** Structure characterizations of $LaSe_2$ nanosheets: (a) the crystal structure of $LaSe_2$. Left part shows a tetragonal ZrSSi-type unit cell divided into three layers, i.e. A, B, and C. In $LaSe_2$, $La^{3+}$, $Se^{2-}$, and $Se^{-}$ occupy Zr- (blue ball), S- (yellow ball) and Si-sites (orange ball), respectively. The cell parameter $a$ for $LaSe_2$ is 4.24 Å. Right-top part shows the top view of A and B layers without distortion. Right-bottom part shows the top view of C layer (planar Se layer), which distorts due to Peierls' theorem. (b) XRD pattern, compared with the standard XRD pattern of orthorhombic $LaSe_2$ (JCPDS no. 19-0651). (c) TEM images. (d) HRTEM images and corresponding FFT pattern (inset). (e) SAED pattern of the $LaSe_2$ nanosheets shown in the inset (scale bar: 200 nm). (f) SAED pattern of the same $LaSe_2$ nanosheets shown in panel (e) obtained at a longer camera length (main diffraction peaks are highlighted by red circles and satellite peaks appear between two main peaks, as indicated by the dashed red line).

The crystal structure of $LaSe_2$ was derived from that of ZrSSi in tetragonal phase. Left part of Figure 1a shows a cell in ZrSSi type. $La^{3+}$ ions occupy the Zr-sites (blue balls), and $Se^{2-}$ ions occupy the S-sites (yellow balls) in layers A and B. Furthermore, Si sites (orange balls) in layer C are also occupied by Se element. To balance the charge in $LaSe_2$ cell, every Se atom on Si-site has to gain one more electron to form $Se^{-}$ ion.[47,48] Since an unpaired electron exists in $Se^{-}$ ions, $Se^{-}$ monolayer will distort due to Peierls' theorem, as illustrated in the lower right part of Figure 1a.

Black line in Figure 1b is the XRD pattern of $LaSe_2$ nanosheets, which is in good accordance with the standard XRD pattern of $LaSe_2$ bulk material (red line, JCPDS no. 19-0651). Calculated from the XRD pattern, the lattice parameters of tetragonal $LaSe_2$ nanosheets were $a = 4.2432(5)$ Å and $c = 8.588(2)$ Å. Figure 1c shows the TEM image of $LaSe_2$ nanosheets. All of the $LaSe_2$ nanosheets show the square shape, and the average side length of the nanosheets is 1.0 ± 0.2 μm. The molar ratio between La and Se obtained from EDX analysis (Figure S1a) is 36:64, which is near the stoichiometric ratio of 1:2. Figure 1d shows the HRTEM image of the edge of a $LaSe_2$ nanosheets, and the inset shows the corresponding fast Fourier transformation (FFT) pattern. The distance between two nearest lattice fringes is 3.00 Å, which equals the spacing between two nearest (110) planes (crystal indices here are defined based on the unit cell shown in the left part of Figure 1a). This indicates that the basal plane of the nanosheet is perpendicular to the $c$ axis of the unit cell, and the edge of the nanosheet is parallel to the $a$ axis.

Figure 1e shows the SAED pattern of a $LaSe_2$ nanosheet shown in the inset, and Figure 1f is an SAED pattern of the same nanosheet obtained at a longer camera length. Main diffraction peaks in Figure 1f are highlighted by red circles. The reciprocal of the length of the red dashed line equals $a/2$, i.e., 2.12 Å. Since the (100) diffraction peaks should disappear due to systematic extinction, only diffraction peaks in red circles should be observed if the atomic arrangement in $LaSe_2$ nanosheets keeps all the symmetry of ZrSSi. The appearance of other diffraction peaks indicates the distortion in layer C and the breaking of the original tetragonal symmetry. Satellite diffraction peaks appear at 1/4 positions between two nearest main diffraction peaks along the [100] direction, indicating that the $Se^{-}$ layers distort into a commensurate modulated structure.

The TEM images of $RESe_2$ (RE = Ce to Nd, Eu) NCs are shown in Figure S2 (the insets show the corresponding SAED patterns). Square nanosheets with side length of 400 ± 30 nm were obtained in the case of $CeSe_2$, while $PrSe_2$ and $NdSe_2$ nanosheets curled into nanotubes with the length of several micrometers. Both of $CeSe_2$ and $PrSe_2$ nanosheets were well crystallized single crystals, while $NdSe_2$ nanosheets were poorly crystallized. $RE_4O_4Se_3$ nanoplates existed as impurities together with $PrSe_2$ and $NdSe_2$ nanosheets. Single-crystalline $EuSe_2$ nanobars with a size distribution from 100 to 350 nm were obtained. The SEM image of $EuSe_2$ nanobars is shown in Figure S3. The results of EDX analyses of these four samples are listed in Figure S1b−e and Table S2. The atomic ratios of RE:Se in $CeSe_2$ and $EuSe_2$ NCs are near the stoichiometric ratio of 1:2 but deviate from this ratio in $PrSe_2$ and $NdSe_2$ NCs, due to the existence of $RE_4O_4Se_3$ nanoplates as impurities. The XRD patterns of these samples are shown in Figure S4. All of these patterns are in accordance with the corresponding standard XRD peaks. In the pattern of $CeSe_2$ nanosheets, the appearance of some extra diffraction peaks may be caused by the modulated ZrSSi-type structure in this sample.

**Spiral Structure of $LaSe_2$ Nanosheets.** Figures 2 and S5 show the TEM, AFM, and SEM images of $LaSe_2$ nanosheets obtained with different growth durations. As shown in these images, the as-synthesized $LaSe_2$ nanosheets are not planar sheets but helicoids, as a result of the spiral growth at screw dislocations. Different from the cases studied by Jin and co-workers,[49] Moire fringes appear in the TEM images (Figures 2a,c and S5c), which indicates that the lattice direction on different layers rotated slightly and spaces existed between different slices on one helicoid. SEM images (Figures 2d,f and S5f) also show that each slice was separated from the upper and lower ones.

Figures 2a,b and S5a,b show the TEM, AFM, and SEM images of the sample taken out from the flask at 1 min after the reaction solution turned black. Square $LaSe_2$ nanosheets with a side length of about 1 μm formed within 1 min of the growth regime. The edge of the nanosheets was very rough. Regions of different contrasts in the TEM images and steps on the upper surface of the nanosheet shown in the AFM image indicate that one as-formed nanosheet here was composed of several thinner slices. The SEM image (Figure S5b) shows that the spiral

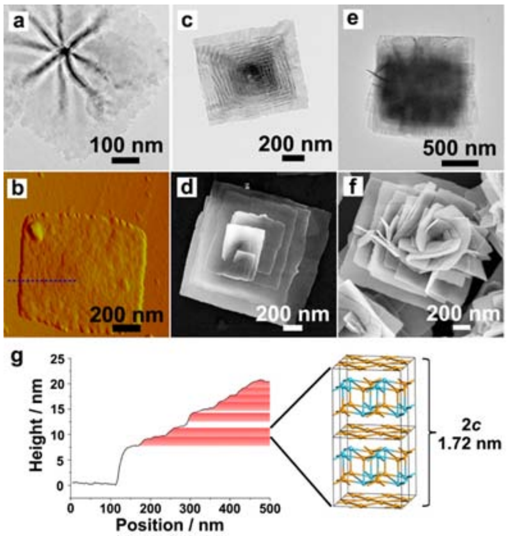

**Figure 2.** Morphology characterization of $LaSe_2$ nanosheets obtained with different growth durations. 1 min: (a) TEM image and (b) AFM phase image; 15 min: (c) TEM and (d) SEM images; 30 min: (e) TEM and (f) SEM images. (g) Height diagram along the blue dashed line in panel b. Every red stripe represents two layers of $LaSe_2$.

structure had formed in this early stage. Figure 2g shows the height diagram along the blue dashed line in Figure 2b. Many steps can be seen in this height diagram. Most of the heights of these steps are approximately equal to or larger than twice of the height of one unit cell of $LaSe_2$, i.e., 1.72 nm, as indicated by the red stripes in Figure 2g. Therefore, it is highly possible that every slice was composed of two layers of cells. Due to the weak layer−layer interaction in $LaSe_2$, solvent molecules might insert into the layered structure of $LaSe_2$ and separate two slices. Consequently, the heights of some steps in Figure 2g are larger than 1.72 nm. The existence of solvent molecules inserted between slices could be confirmed by removing these inserted molecules by thermal treatment followed by measuring the change in step height. Figure S6 shows an AFM image of $LaSe_2$ nanosheets (growth duration: 1 min) after thermal treatment at 300 °C in air for 30 min, and Figure S7 compares the statistical results of the height of steps on $LaSe_2$ nanosheets before and after thermal treatment obtained from AFM measurements. It can be seen that the steps higher than 2.2 nm disappeared after thermal treatment, indicating the removal of the solvent molecules inserted between slices.

Figures 2c,d and S5c,d show the TEM and SEM images of $LaSe_2$ nanosheets obtained after growing for 15 min. Spiral structure was well-developed in these nanosheets and distinct Moire fringes can be seen in the TEM images. In some cases, several centers of screw dislocation exist in one nanosheet, as shown in Figures 2d and S5c,d. As a result of ripening process, the edge of the nanosheets became smoother as the growth time extended. If the growth period was further extended to 30 min, the newly formed slices would roll up, and the nanosheets would grow into rose-shaped NCs, as shown in Figures 2e,f and S5e,f.

**Structure Characterization of $RE_4O_4Se_3$ Nanoplates.** $RE_4O_4Se_3$ (RE = La to Nd, Sm) bulk materials (orthorhombic phase) have been reported earlier by other groups.[28,29,50] Similar to $RESe_2$, the crystal structure of $RE_4O_4Se_3$ also shows layered feature. As shown in Figure 3, two kinds of basic layers, $_\infty\{[RE_4O_4]^{4+}\}$ layers and $_\infty\{[Se_3]^{4-}\}$ layers, alternately build up the crystals. $_\infty\{[RE_4O_4]^{4+}\}$ layers are formed by $[ORE_4]^{10+}$ tetrahedrons with common edges and $_\infty\{[Se_3]^{4-}\}$ layers by parallel Se chains composed of $Se^{2-}$ ions and $[Se-Se]^{2-}$ dumbbells. It is predictable that if the ionic radii of $RE^{3+}$ ions decrease, the unit cell will shrink on $x$ direction, resulting in the interaction between $Se^{2-}$ ions and $[Se-Se]^{2-}$ dumbbells.

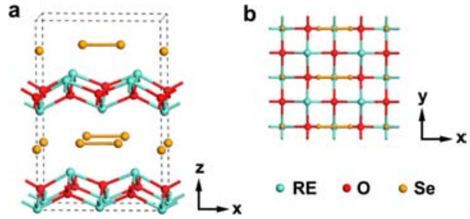

**Figure 3.** Crystal structure of orthorhombic $RE_4O_4Se_3$: (a) side and (b) top views.

With the method presented in the Experimental Section, $RE_4O_4Se_3$ (RE = Pr, Nd, Sm, Gd to Ho) nanoplates could be obtained together with $RESe_2$ nanosheets or some amorphous membranous impurities. Therefore, low-speed centrifugation procedure was needed to separate $RE_4O_4Se_3$ nanoplates from those byproducts with larger sizes. However, since the yield of $Pr_4O_4Se_3$ nanoplates was quite low and most of $Pr_4O_4Se_3$ nanoplates were rolled up in $PrSe_2$ nanosheets, it was very hard to get powder sample of $Pr_4O_4Se_3$ nanoplates separated from $PrSe_2$ nanosheets. Figure S8 shows the TEM images, SAED pattern, and EDS analysis of the mixed sample of $PrSe_2$ nanosheets and $Pr_4O_4Se_3$ nanoplates. The SAED pattern of $Pr_4O_4Se_3$ nanoplates was similar to those of other $RE_4O_4Se_3$ nanoplates, confirming that the nanoplates were orthorhombic $Pr_4O_4Se_3$. The atomic ratio of Pr:Se was 42:58, indicating the existence of the mixture of $PrSe_2$ and $Pr_4O_4Se_3$. Thus $Pr_4O_4Se_3$ nanoplates will not be discussed in the following paragraphs. The powder samples of $Nd_4O_4Se_3$ and $Sm_4O_4Se_3$ were brown, while other four samples showed very dark violet color. Calculated from ICP-AES results, the yields of $NdSe_2$ nanosheets and $Nd_4O_4Se_3$ and $Gd_4O_4Se_3$ nanoplates were 62.8%, 28.3%, and 46.7%, respectively.

Figure 4 shows the TEM images and corresponding SAED patterns of $RE_4O_4Se_3$ nanoplates. All of these nanoplates show near square shape. The size distributions of these nanoplates are listed in Table 1. As the RE element changes from light to heavy RE, the size of $RE_4O_4Se_3$ nanoplates became smaller, and the thickness became thinner. Meanwhile, their SAED patterns show systematic outward shifts, indicating that these RE oxyselenide share similar crystal structure and the lattice shrinks from $Nd_4O_4Se_3$ to $Ho_4O_4Se_3$. The results of corresponding EDS analyses are shown in Table 1 and Figure S9. The atomic ratios of RE:Se of these nanoplates were close to their stoichiometric ratio of 4:3.

From $Nd_4O_4Se_3$ to $Ho_4O_4Se_3$, the gradual decreasing of the Se element may be caused by a gradual increasing of the concentration of Se vacancies in the nanoplates. The atomic ratio of O:Se in the lattice of $RE_4O_4Se_3$ nanoplates could be estimated from the results of C−H−N elemental analysis (Table S4) and XPS analysis (Table S5) of the nanoplates. The amount of OA adsorbed on nanoplates could be obtained from C−H−N elemental analysis, and the atomic ratio of C:O:Se could be obtained from XPS analysis. After subtracting the contribution from the oxygen atoms in OA, the atomic ratios of O:Se in the lattices of $Nd_4O_4Se_3$ and $Gd_4O_4Se_3$ nanoplates

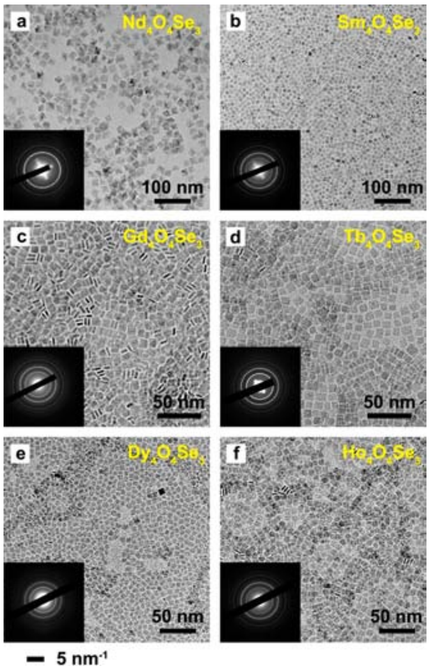

**Figure 4.** TEM images and corresponding SAED patterns (insets) of the nanoplates of (a) $Nd_4O_4Se_3$, (b) $Sm_4O_4Se_3$, (c) $Gd_4O_4Se_3$, (d) $Tb_4O_4Se_3$, (e) $Dy_4O_4Se_3$, (f) $Ho_4O_4Se_3$.

**Table 1. Size Distributions and Elemental Analysis Results of $RE_4O_4Se_3$ Nanoplates**

| | side length (nm) | thickness (nm) | atomic ratio of RE:Se |
|---|---|---|---|
| $Nd_4O_4Se_3$ | 20 ± 2 | 3.5 ± 0.4 | 52:48 |
| $Sm_4O_4Se_3$ | 10.3 ± 0.9 | 3.2 ± 0.4 | 54:46 |
| $Gd_4O_4Se_3$ | 8.5 ± 0.7 | 2.7 ± 0.3 | 55:45 |
| $Tb_4O_4Se_3$ | 8.3 ± 0.8 | 1.7 ± 0.2 | 59:41 |
| $Dy_4O_4Se_3$ | 6.4 ± 0.7 | 1.9 ± 0.2 | 60:40 |
| $Ho_4O_4Se_3$ | 7.9 ± 0.7 | 2.1 ± 0.2 | 64:36 |

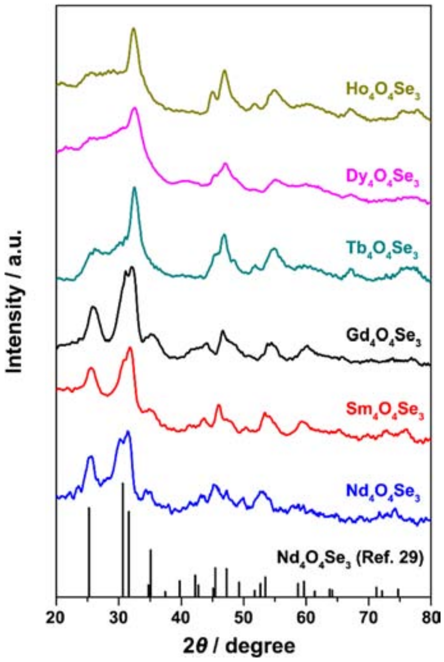

**Figure 5.** XRD patterns of $RE_4O_4Se_3$ (RE = Nd, Sm, Gd to Ho) nanoplates, compared with the XRD pattern of bulk $Nd_4O_4Se_3$ calculated from the crystallographic data reported in ref 29.

were calculated to be 1.0:1 and 1.2:1, respectively, which were close to the stoichiometric ratio of 4:3.

Figure 5 shows the XRD patterns of $RE_4O_4Se_3$ nanoplates compared with that of $Nd_4O_4Se_3$ bulk material, which was calculated from previously reported crystallographic data[29] (using PowderCell for Windows, version 2.4). The indices of the calculated diffraction peaks are listed in Table S3. The XRD pattern of $Nd_4O_4Se_3$ nanoplates can match the calculated one. The diffraction peaks of other $RE_4O_4Se_3$ nanoplates show gradual systematic shifts toward high angle, indicating the lattice contraction caused by the decreasing of the ionic radii from $Nd^{3+}$ to $Ho^{3+}$. However, the crystal structures for $RE_4O_4Se_3$ (RE = Gd to Ho) have not been reported, they cannot be solved from the nanoplates samples due to the broadening of the diffraction peaks. Supposing $RE_4O_4Se_3$ (RE = Gd to Ho) crystals possess the same orthorhombic crystal structure as $Nd_4O_4Se_3$ and can be described by the model shown in Figure 3, the lattice parameters of $Gd_4O_4Se_3$ are $a$ = 8.2412(5) Å, $b$ = 3.9298(2) Å, and $c$ = 12.5311(8) Å, which were calculated from 10 strongest diffraction peaks in the XRD pattern of $Gd_4O_4Se_3$ nanoplates. Compared with the lattice parameters of $Nd_4O_4Se_3$ ($a$ = 8.4568(4) Å, $b$ = 3.9883(2) Å, $c$ = 12.8245(7) Å), the unit cell of $Gd_4O_4Se_3$ was compressed. Since $Tb_4O_4Se_3$, $Dy_4O_4Se_3$, and $Ho_4O_4Se_3$ nanoplates were smaller and thinner than other $RE_4O_4Se_3$ nanoplates and contained high concentration of Se vacancies, some weak diffraction peaks cannot be observed in their XRD patterns.

Figure 6 shows the top- and side-view HRTEM images of $Nd_4O_4Se_3$ and $Gd_4O_4Se_3$ nanoplates. Although $Nd_4O_4Se_3$ and $Gd_4O_4Se_3$ nanoplates were similar in crystal structure and morphology, the growth directions of these two kinds of nanoplates were different. Considering the layered structure of $RE_4O_4Se_3$ shown in Figure 3, it is very likely that the nanoplates expose (001) and (00−1) facets as the upper and lower

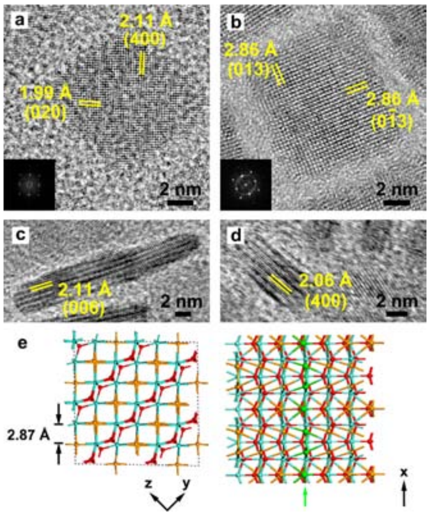

**Figure 6.** Growth directions of $Nd_4O_4Se_3$ and $Gd_4O_4Se_3$ nanoplates. Top (a and b) and side (c and d) view HRTEM images of $Nd_4O_4Se_3$ (a and c) and $Gd_4O_4Se_3$ (b and d) nanoplates are shown. FFT patterns of the top view images are shown in the corresponding insets. The interplanar spacing and corresponding indices are marked on the images. (e) Structure model of $Gd_4O_4Se_3$ nanoplates: left is the top view and right is the side view. A Se chain in the side view is highlighted by green color.

surfaces, which was the case for $Nd_4O_4Se_3$ nanoplates. The side surfaces of $Nd_4O_4Se_3$ nanoplates were {210} facets. However, each $Gd_4O_4Se_3$ nanoplate exposed two {100} facets as the upper and lower surfaces and four {013} facets as the side surfaces. Figure 6e schematically shows the structure of $Gd_4O_4Se_3$ nanoplates. In this structure, Se chains are perpendicular to the upper and lower surfaces. This structure may be caused by a relatively low growth rate of Se chains in the compressed lattice of $Gd_4O_4Se_3$ compared with that of $Nd_4O_4Se_3$. Since the {013} facets of $Gd_4O_4Se_3$ possess the maximum atomic density, thus low surface energy, these facets were exposed as the side surfaces of $Gd_4O_4Se_3$ nanoplates.

**Formation Conditions for $RESe_2$ and $RE_4O_4Se_3$ NCs Along RE Series.** $RE(acac)_3$ (RE = La, Pr, Nd, Sm to Ho) and $Ce(Ac)_3$ were used as precursors of RE elements in this work, which were also used in the synthesis of RE oxide,[31] oxysulfide,[39−41] and $NaRES_2$[46] NCs. These precursors could transform into RE oleate under vacuum in the mixed solvent of OA, OM, and ODE. Then RE monomers could be released steadily as the oleate decomposed at 310 °C. Moreover, using $SeO_2$ as the precursor of Se was another key factor in the synthesis of $RESe_2$ and $RE_4O_4Se_3$ NCs. $SeO_2$ could be easily reduced by OM and dissolved in solvent, and it was possible to prepare NCs contain Se (−1) in this condition.

The structures of $RESe_2$ and $RE_4O_4Se_3$ are both layered structure containing Se layers. In $RESe_2$, Se layers with Se (−1) grids are sandwiched between $_\infty\{[RESe]^+\}$ layers. The $_\infty\{[RESe]^+\}$ layers can be regarded as $[SeRE_5]^{13+}$ square pyramids with shared edges. In $RE_4O_4Se_3$, Se layers consisting of $-Se^{2-}-[Se-Se]^{2-}-$ chains are sandwiched between $_\infty\{[RE_4O_4]^{4+}\}$ layers. Figure 7 schematically shows the formation competition between $RESe_2$ and $RE_4O_4Se_3$. Whether $RESe_2$ or $RE_4O_4Se_3$ NCs would be obtained was decided by the properties of $RE^{3+}$ ions and the reaction conditions. Since the ionic radii of the trivalent ions decrease from La to Lu, according to the HSAB theory, the affinity of $RE^{3+}$ ions toward $Se^{2-}$ ions weakens, while that toward $O^{2-}$ ions strengthens. Consequently, $_\infty\{[RESe]^+\}$ layers of light RE elements could form in $RESe_2$ NCs, while only $_\infty\{[RE_4O_4]^{4+}\}$ layers could form for middle RE elements in $RE_4O_4Se_3$ NCs. Furthermore, the crystallinity of $LaSe_2$ nanosheets and $Nd_4O_4Se_3$ nanoplates was much better than that of $NdSe_2$ nanosheets and $Ho_4O_4Se_3$ nanoplates, respectively, as shown in the XRD patterns. High concentration of Se vacancies in $Dy_4O_4Se_3$ and $Ho_4O_4Se_3$ nanoplates is another consequence of the weak affinity between Se and Dy or Ho. All of these phenomena strongly suggest that the bonding between Se and light RE was more thermodynamically favored than that between Se and middle or heavy RE.

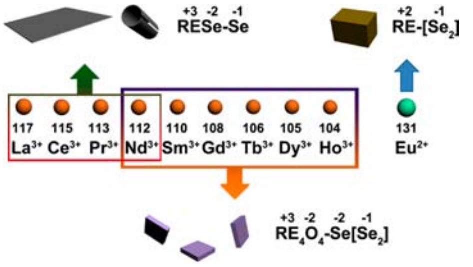

**Figure 7.** Formation competition between $RESe_2$ and $RE_4O_4Se_3$ based on HSAB theory. The values on the element symbols are the ionic radii of the corresponding ions (unit, pm).

Another reason for the formation of Se vacancies in $Dy_4O_4Se_3$ and $Ho_4O_4Se_3$ nanoplates is that, due to the smaller size of $Dy^{3+}$ and $Ho^{3+}$ ions compared with trivalent ions of light RE, the unit cells of $Dy_4O_4Se_3$ and $Ho_4O_4Se_3$ are more compressed and too crowded for $Se^{2-}$ ions and $[Se-Se]^{2-}$ dumbbells, resulting in the escape of some Se atoms from the lattice.

While the formation of $EuSe_2$ nanobars instead of $Eu_4O_4Se_3$ nanoplates seems an exception of the trend we discussed above, this result is comprehensible because the crystal structure of $EuSe_2$ (tetragonal phase) is totally different from that of other $RESe_2$,[51] as shown in Figure S10. Eu atoms are divalent in $EuSe_2$, and previous works have shown that the divalent RE ions are much softer compared to trivalent ones, leading to higher affinity to soft bases, i.e., S[43] and Se.[44,45]

In addition, if Na(acac) (3 mmol) was introduced into the reaction solution together with $RE(acac)_3$, $NaRESe_2$ (RE = La, Ce) NCs in cubic phase could be obtained, similar to $NaRES_2$ NCs in our previous report.[46] The XRD patterns and TEM images of $NaRESe_2$ are shown in Figure S11 and S12, respectively. Calculated from EDS results in Figure S13, the atomic ratios of Na:RE:Se are 18:26:56 for $NaLaSe_2$ NCs and 16:28:56 for $NaCeSe_2$ NCs.

**Electronic Transport Property of $LaSe_2$ Nanosheet Films.** Lots of RE compounds containing 2D sheets of Se or Te atoms are considered as 2D charge density wave conductor with special electronic transport properties. For instance, $LaSeTe_2$ exhibit metal-semiconductor transition at about 270 K.[26] The resistivity of $LaSeTe_2$ powder was about 0.9 Ω·cm at 300 K and reached the minimum value of 0.7 Ω·cm at 270 K. When the temperature decreased to 4 K, the resistivity increased to 1.4 Ω·cm.

Herein, two $LaSe_2$ films with good electrical conductivity were fabricated by drop-casting the cyclohexane dispersion of $LaSe_2$ nanosheets on $SiO_2$ substrates. Thermal treatment at 300 °C in air was used to remove the organic ligands adsorbed on the surface of the nanosheets. As shown in the XRD pattern (Figure S14) and TEM image (Figure S15) of $LaSe_2$ nanosheets after the thermal treatment for 30 min, the as-synthesized $LaSe_2$ nanosheets were stable under this procedure. Figure S16 shows the IR spectra of $LaSe_2$ nanosheets before and after the thermal treatment. The stretching vibrational peaks of C−H bonds around 2800 $cm^{-1}$ dropped dramatically, which indicates that most of the OA and OM molecules adsorbed on the surface of $LaSe_2$ nanosheets were successfully removed. Four-electrode method was used to measure the resistivity of the $LaSe_2$ nanosheet films under different currents. The result of the resistivity measurements of these two films was repeatable, as shown in Figure 8. When the current that went through the films increased, the resistivity of the films decreased. According to the definition of resistivity:

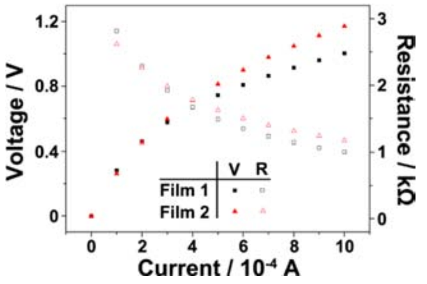

**Figure 8.** Resistance measurement of two $LaSe_2$ nanosheet films.

$$\rho = \frac{b \cdot h}{l} R \tag{1}$$

where $b$, $h$ and $l$ represent the width, thickness and length of the channel, respectively, and $R$ stands for the resistance of the film, the resistivity of as-prepared $LaSe_2$ films ranged from 3.4 to 1.1 Ω·cm as the current increased from 0.1 to 1.0 mA. These values are comparable in magnitude with the resistivity of bulk $LaSeTe_2$,[26] which possesses similar structure with $LaSe_2$. Because the interfacial resistance between $LaSe_2$ nanosheets contributed a lot to the total resistance of the films, the intrinsic resistivity of $LaSe_2$ nanosheets is significantly lower than the values listed above, and the nonohmic contact between $LaSe_2$ nanosheets is a possible reason for the nonlinear $I-V$ relationship shown in Figure 8. Due to their comparatively large size (1 $\mu$m) and low resistivity (<1 Ω·cm), $LaSe_2$ nanosheets are ideal candidates to fabricate nanofield-effect transistor[9,10] and in-plane supercapacitor.[11]

**Light Extinction Property of $RE_4O_4Se_3$ Nanoplates.** Figure 9b shows the photo of the cyclohexane dispersion of $RE_4O_4Se_3$ (RE = Nd, Sm, Gd to Ho) nanoplates. The dispersions of $Nd_4O_4Se_3$ and $Sm_4O_4Se_3$ nanoplates present similar brown colors, and the dispersions of the other four kinds of $RE_4O_4Se_3$ nanoplates appear similar violet colors. Figure 9a shows the absorption spectra of these samples. Two main peaks below 3 eV were observed in the spectrum of $Sm_4O_4Se_3$ dispersion, while only one obvious peak could be seen in the spectra of other samples.

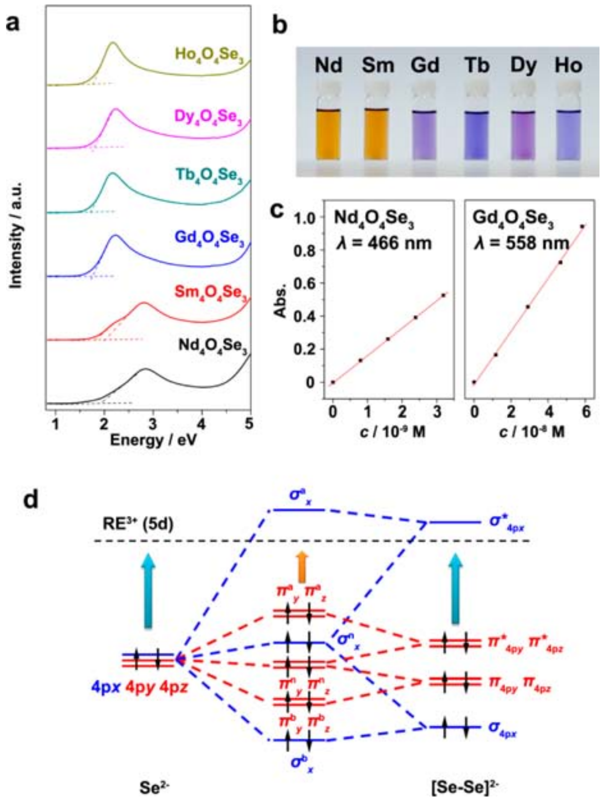

Figure 9. Light extinction property of the cyclohexane dispersions of $RE_4O_4Se_3$ nanoplates: absorption spectra (a) and photos (b) of $RE_4O_4Se_3$ nanoplates dispersions. (c) Absorbance of the dispersions of $Nd_4O_4Se_3$ nanoplates and $Gd_4O_4Se_3$ nanoplates at corresponding maximum absorption wavelength depends on the concentrations of nanoplates. (d) Scheme of the interaction between $Se^{2-}$ ion and $[Se-Se]^{2-}$ dumbbell along $x$ direction in vacuum. Blue and red lines show $\sigma$- and $\pi$-interactions, respectively. The superscripts, b, n and a, stand for bonding, nonbonding, and antibonding, respectively. The energy level of RE (5d) is marked with black dashed line.

The absorption edge energy ($E_g$) of each peak was defined as the energy of the intersection point of the spectral baseline along the energy axis and the extrapolated line of the linear part at the lower-energy side of the peak, as illustrated by the dashed lines in Figure 9a. $E_g$ of each peak was listed in Table 2. These peaks could be divided into two classes according to $E_g$ values: peaks with $E_g$ about 1.95 eV and peaks with $E_g$ between 1.73 and 1.79 eV. $E_g$ with lower energy here can be assigned to the optical band gap of the sample. According to former report,[29] the optical band gaps of $RE_4O_4Se_3$ (RE = La, Pr, Nd, Sm) bulk materials were ~1.9 eV. It is comprehensive, due to the small-size effect, the band gap of $Nd_4O_4Se_3$ nanoplates was wider than that of the bulk counterpart. But the band gap of other $RE_4O_4Se_3$ nanoplates decreased.

Table 2. Absorption Edge Energy of Each Peak in the Absorption Spectra of the Dispersions of $RE_4O_4Se_3$ Nanoplates

| | $E_g$ (eV) |
|---|---|
| $Nd_4O_4Se_3$ | 1.95 |
| $Sm_4O_4Se_3$ | 1.79, 1.96 |
| $Gd_4O_4Se_3$ | 1.74 |
| $Tb_4O_4Se_3$ | 1.73 |
| $Dy_4O_4Se_3$ | 1.78 |
| $Ho_4O_4Se_3$ | 1.73 |

Herein, we attribute this abnormal phenomenon to the interaction between $Se^{2-}$ ions and $[Se-Se]^{2-}$ dumbbells. In the former report,[29] the top of the valence band and the bottom of the conduction band were attributed to Se (4p) states and RE (5d) states, respectively. The as-mentioned Se (4p) states may come from the Se (4p) orbitals of $Se^{2-}$ ions or $[Se-Se]^{2-}$ dumbbells. The interaction between $Se^{2-}$ ions and $[Se-Se]^{2-}$ dumbbells can result in the rise of energy of the top of the valence band. Figure 9d schematically shows the interaction between the 4p orbitals of $Se^{2-}$ ions and $[Se-Se]^{2-}$ dumbbells along $x$ direction in vacuum. Since the energy of $\pi^a{}_y$ and $\pi^a{}_z$, the highest occupied orbitals in interaction case, is higher than the energy of 4p orbitals of isolated $Se^{2-}$ ions or $\pi^*{}_{4p}$ orbitals of $[Se-Se]^{2-}$ dumbbells, the energy gap between Se (4p) and RE (5d) decreases as $Se^{2-}$ ions interact with $[Se-Se]^{2-}$ dumbbells. Considering the periodicity of the crystal, every energy level in Figure 9d will generate a band, but the band gap will still be smaller in the interaction case than in the noninteraction case. In $Nd_4O_4Se_3$, the distance between $Se^{2-}$ ions and $[Se-Se]^{2-}$ dumbbells is relatively large. Therefore, $Se^{2-}$ ions cannot interact effectively with $[Se-Se]^{2-}$ dumbbells. When $Nd^{3+}$ ions here are replaced by middle $RE^{3+}$ ions with smaller ionic radii, the lattice of $RE_4O_4Se_3$ will shrink, leading to stronger interaction between $Se^{2-}$ ions and $[Se-Se]^{2-}$ dumbbells. Consequently, the optical band gaps of $RE_4O_4Se_3$ (RE = Sm, Gd to Ho) nanoplates were smaller than that of $Nd_4O_4Se_3$ nanoplates. Interaction and noninteraction cases may exist simultaneously in $Sm_4O_4Se_3$ nanoplates, resulting in the appearance of two absorption peaks. Considering that $\sigma^n{}_x$ orbital, an occupied orbital in the interaction case, partially comes from $\sigma^*{}_{4p_x}$ orbital, an antibonding orbital of $[Se-Se]^{2-}$ dumbbells, the interaction between $Se^{2-}$ ions and $[Se-Se]^{2-}$

dumbbells would weaken and stretch the Se−Se bond in [Se−Se]$^{2-}$ dumbbells. This inference was tested by density functional theory simulation. Figure S17 shows the optimized structure of $Gd_4O_4Se_3$ crystal. Compared with the crystal structure of $Nd_4O_4Se_3$, the unit cell of $Gd_4O_4Se_3$ was compressed on $x$ direction, but the Se−Se bond length in [Se−Se]$^{2-}$ dumbbells increased.

The as-synthesized $RE_4O_4Se_3$ nanoplates exhibit high light extinction ability in the visible light region. Figure 9c show the diagrams of the peak absorbance for each sample depending on the concentrations of $Nd_4O_4Se_3$ and $Gd_4O_4Se_3$ nanoplates in the cyclohexane dispersions. The concentrations of nanoplates here were calculated from the concentration of $Nd^{3+}$ and $Gd^{3+}$ ions obtained from ICP-AES analysis and the average volume of a single $Nd_4O_4Se_3$ or $Gd_4O_4Se_3$ nanoplate obtained from the TEM images. According to Lambert−Beer's law, the molar extinction coefficients of $Nd_4O_4Se_3$ and $Gd_4O_4Se_3$ nanoplates were calculated to be 1.6 × $10^8$ and 1.6 × $10^7$ $M^{-1}\cdot cm^{-1}$, respectively. The intrinsic absorption coefficient $\mu_i$ was defined as

$$\mu_i = \frac{\ln 10}{N_A \cdot V_{NC}}\varepsilon \qquad (2)$$

In this equation, $N_A$, $V_{NC}$, and $\varepsilon$ stand for Avogadro constant, the volume of a single NC, and the molar extinction coefficient of the NCs, respectively.[52] $\mu_i$ of $Nd_4O_4Se_3$ and $Gd_4O_4Se_3$ nanoplates was 4.4 × $10^5$ and 3.1 × $10^5$ $cm^{-1}$, respectively. These values are higher than $\mu_i$ of various quantum dots, such as PbS[53] and CdSe,[54] and comparable to that of $CuInS_2$ (5 × $10^5$ $cm^{-1}$),[55] in the visible light region. Thus, $RE_4O_4Se_3$ nanoplates have potential application in light filters and solar cells.

## CONCLUSIONS

Two types of 2D NCs of trivalent RE selenides and oxyselenides, namely $RESe_2$ nanosheets (RE = La to Nd, for $EuSe_2$, nanobars were obtained) and $RE_4O_4Se_3$ nanoplates (RE = Nd, Sm, Gd to Ho), could be synthesized in mixed solvents of OA-OM-ODE. $SeO_2$ could be used as efficient Se source in the reaction. Both kinds of these NCs contain Se layers involving Se atoms in −1 valence. Since trivalent ions of middle RE, compared with that of light RE, possess stronger affinity toward $O^{2-}$ ions but weaker affinity toward $Se^{2-}$ ions, according to HSAB theory, $RESe_2$ nanosheets were obtained for light RE (La to Nd), and $RE_4O_4Se_3$ nanoplates were obtained for middle RE (Nd, Sm, Gd to Ho). $EuSe_2$ nanobar was an exception because Eu atoms were divalent in this material. $LaSe_2$ nanosheets with a side-length about 1 $\mu$m could form from the screw dislocation driven growth. The number of slices in one nanosheet increased as the reaction duration was prolonged. Satellite diffraction peaks were observed in the SAED pattern of $LaSe_2$ nanosheets, indicating the modulated structure in Se layers. $LaSe_2$ nanosheet films fabricated by drop-casting displayed low electronic resistance at room temperature. The light absorption property of $RE_4O_4Se_3$ nanoplates was characterized. $RE_4O_4Se_3$ nanoplates exhibited high light extinction ability in the visible light region. The optical band gap of $Nd_4O_4Se_3$ nanoplates was broader than that of the bulk counterpart, while those of other $RE_4O_4Se_3$ nanoplates were narrower. We ascribe this phenomenon to the interaction between $Se^{2-}$ ions and [Se−Se]$^{2-}$ dumbbells in the Se layers caused by the lattice shrinkage from $Nd_4O_4Se_3$ to $Gd_4O_4Se_3$.

Since numerous fascinating phenomena have been discovered in different layer-structured selenide compounds, it is of great interest to study the behaviors of these materials on nanoscale. The synthesis method of $RESe_2$ nanosheets and $RE_4O_4Se_3$ nanoplates developed in this work could guide the large-scale synthesis of 2D NCs of other selenide compounds, laying the foundation of the development of new types of transistors, thermoelectric devices, and wave-absorbing materials.

## ASSOCIATED CONTENT

### Ⓢ Supporting Information

The detailed reaction conditions for the syntheses of different NCs, more TEM, SEM, AFM images, EDS analyses, XRD and IR spectra, structure models, and DFT calculation results. This material is available free of charge via the Internet at http://pubs.acs.org.

## AUTHOR INFORMATION

### Corresponding Author

ywzhang@pku.edu.cn; yan@pku.edu.cn

### Present Address

[†]Department of Materials Science and Engineering, Massachusetts Institute of Technology, Cambridge, Massachusetts 02139, U.S.A.

### Author Contributions

[‡]These authors contributed equally.

### Notes

The authors declare no competing financial interest.

## ACKNOWLEDGMENTS

This work was supported by the NSFC (grant nos. 21025101 and 21271011). The authors thank Mr. Lu-Wei Zhong for the help in the AFM characterization. Y.W.Z. particularly appreciates the financial aid of China National Funds for Distinguished Young Scientists from the NSFC.

## REFERENCES

(1) Yang, J.; Son, J. S.; Yu, J. H.; Joo, J.; Hyeon, T. *Chem. Mater.* **2013**, *25*, 1190.

(2) Bouet, C.; Tessier, M. D.; Ithurria, S.; Mahler, B.; Nadal, B.; Dubertret, B. *Chem. Mater.* **2013**, *25*, 1262.

(3) Zhang, H. J.; Liu, C. X.; Qi, X. L.; Dai, X.; Fang, Z.; Zhang, S. C. *Nat. Phys.* **2009**, *5*, 438.

(4) Kwon, S. K.; Youn, S. J.; Min, B. I. *Phys. Rev. B* **2000**, *62*, 357.

(5) Morosan, E.; Natelson, D.; Nevidomskyy, A. H.; Si, Q. *Adv. Mater.* **2012**, *24*, 4896.

(6) Dimasi, E.; Aronson, M. C.; Mansfield, J. F.; Foran, B.; Lee, S. *Phys. Rev. B* **1995**, *52*, 14516.

(7) Gweon, G. H.; Denlinger, J. D.; Clack, J. A.; Allen, J. W.; Olson, C. G.; DiMasi, E.; Aronson, M. C.; Foran, B.; Lee, S. *Phys. Rev. Lett.* **1998**, *81*, 886.

(8) Guo, J.; Jin, S.; Wang, G.; Wang, S.; Zhu, K.; Zhou, T.; He, M.; Chen, X. *Phys. Rev. B* **2010**, 82.

(9) Radisavljevic, B.; Radenovic, A.; Brivio, J.; Giacometti, V.; Kis, A. *Nat. Nanotechnol.* **2011**, *6*, 147.

(10) Kong, D.; Dang, W.; Cha, J. J.; Li, H.; Meister, S.; Peng, H.; Liu, Z.; Cui, Y. *Nano Lett.* **2010**, *10*, 2245.

(11) Feng, J.; Sun, X.; Wu, C.; Peng, L.; Lin, C.; Hu, S.; Yang, J.; Xie, Y. *J. Am. Chem. Soc.* **2011**, *133*, 17832.

(12) Hor, Y. S.; Richardella, A.; Roushan, P.; Xia, Y.; Checkelsky, J. G.; Yazdani, A.; Hasan, M. Z.; Ong, N. P.; Cava, R. J. *Phys. Rev. B* **2009**, 79.

(13) Joo, J.; Son, J. S.; Kwon, S. G.; Yu, J. H.; Hyeon, T. *J. Am. Chem. Soc.* **2006**, *128*, 5632.

(14) Ithurria, S.; Dubertret, B. *J. Am. Chem. Soc.* **2008**, *130*, 16504.

(15) Zhang, X.; Zhang, J.; Zhao, J.; Pan, B.; Kong, M.; Chen, J.; Xie, Y. *J. Am. Chem. Soc.* **2012**, *134*, 11908.

(16) Jeong, S.; Yoo, D.; Jang, J.-t.; Kim, M.; Cheon, J. *J. Am. Chem. Soc.* **2012**, *134*, 18233.

(17) Schliehe, C.; Juarez, B. H.; Pelletier, M.; Jander, S.; Greshnykh, D.; Nagel, M.; Meyer, A.; Foerster, S.; Kornowski, A.; Klinke, C.; Weller, H. *Science* **2010**, *329*, 550.

(18) Ithurria, S.; Tessier, M. D.; Mahler, B.; Lobo, R. P. S. M.; Dubertret, B.; Efros, A. L. *Nat. Mater.* **2011**, *10*, 936.

(19) Kirkeminde, A.; Ruzicka, B. A.; Wang, R.; Puna, S.; Zhao, H.; Ren, S. *ACS Appl. Mater. Interfaces* **2012**, *4*, 1174.

(20) Park, K. H.; Jang, K.; Son, S. U. *Angew. Chem., Int. Ed.* **2006**, *45*, 4608.

(21) Vaughn, D. D.; In, S.-I.; Schaak, R. E. *ACS Nano* **2011**, *5*, 8852.

(22) Bottcher, P.; Doert, T.; Arnold, H.; Tamazyan, R. *Z. Kristallogr.* **2000**, *215*, 246.

(23) Bartsch, C.; Doert, T. *J. Solid State Chem.* **2012**, *185*, 101.

(24) Dashjav, E.; Oeckler, O.; Doert, T.; Mattausch, H.; Bottcher, P. *Angew. Chem., Int. Ed.* **2000**, *39*, 1987.

(25) Doert, T.; Tsinde, B. P. F.; Lidin, S.; Garcia, F. J. G. *J. Solid State Chem.* **2004**, *177*, 1598.

(26) Doert, T.; Fokwa, B. P. T.; Simon, P.; Lidin, S.; Söhnel, T. *Chem.—Eur. J.* **2003**, *9*, 5865.

(27) Tsinde, B. P. F.; Doert, T. *Solid State Sci.* **2005**, *7*, 573.

(28) Weber, F. A.; Schleid, T. *Z. Anorg. Allg. Chem.* **2001**, *627*, 1383.

(29) Strobel, S.; Choudhury, A.; Dorhout, P. K.; Lipp, C.; Schleid, T. *Inorg Chem.* **2008**, *47*, 4936.

(30) Cao, Y. C. *J. Am. Chem. Soc.* **2004**, *126*, 7456.

(31) Si, R.; Zhang, Y.-W.; You, L.-P.; Yan, C.-H. *Angew. Chem., Int. Ed.* **2005**, *44*, 3256.

(32) Zhang, Y.-W.; Sun, X.; Si, R.; You, L.-P.; Yan, C.-H. *J. Am. Chem. Soc.* **2005**, *127*, 3260.

(33) Wang, X.; Zhuang, J.; Peng, Q.; Li, Y. *Inorg. Chem.* **2006**, *45*, 6661.

(34) Mai, H.-X.; Zhang, Y.-W.; Si, R.; Yan, Z.-G.; Sun, L.-d.; You, L.-P.; Yan, C.-H. *J. Am. Chem. Soc.* **2006**, *128*, 6426.

(35) Boyer, J.-C.; Cuccia, L. A.; Capobianco, J. A. *Nano Lett.* **2007**, *7*, 847.

(36) Du, Y.-P.; Zhang, Y.-W.; Yan, Z.-G.; Sun, L.-D.; Yan, C.-H. *J. Am. Chem. Soc.* **2009**, *131*, 16364.

(37) Du, Y.-P.; Zhang, Y.-W.; Sun, L.-D.; Yan, C.-H. *J. Am. Chem. Soc.* **2009**, *131*, 3162.

(38) Zhao, F.; Yuan, M.; Zhang, W.; Gao, S. *J. Am. Chem. Soc.* **2006**, *128*, 11758.

(39) Ding, Y.; Gu, J.; Ke, J.; Zhang, Y.-W.; Yan, C.-H. *Angew. Chem., Int. Ed.* **2011**, *50*, 12330.

(40) Zhang, T.; Gu, J.; Ding, Y.; Zhang, Y.-W.; Yan, C.-H. *ChemPlusChem* **2013**, DOI: 10.1002/cplu.201300092.

(41) Gu, J.; Ding, Y.; Ke, J.; Zhang, Y.-W.; Yan, C.-H. *Acta Chim. Sinica* **2013**, *71*, 360.

(42) Pearson, R. G. *Science* **1966**, *151*, 172.

(43) Zhao, F.; Sun, H. L.; Su, G.; Gao, S. *Small* **2006**, *2*, 244.

(44) Tanaka, A.; Adachi, T.; Hasegawa, Y.; Kawai, T. *J. Alloys Comp.* **2009**, *488*, 538.

(45) Hasegawa, Y.; Adachi, T.-A.; Tanaka, A.; Afzaal, M.; O'Brien, P.; Doi, T.; Hinatsu, Y.; Fujita, K.; Tanaka, K.; Kawai, T. *J. Am. Chem. Soc.* **2008**, *130*, 5710.

(46) Ding, Y.; Gu, J.; Zhang, T.; Yin, A.-X.; Yang, L.; Zhang, Y.-W.; Yan, C.-H. *J. Am. Chem. Soc.* **2012**, *134*, 3255.

(47) Benazeth, S.; Carre, D.; Laruelle, P. *Acta Crystallogr., Sect. B: Struct. Sci.* **1982**, *38*, 33.

(48) Grzechnik, A.; Zheng, J. Z.; Wright, D.; Petuskey, W. T.; McMillan, P. F. *J. Phys. Chem. Solids* **1996**, *57*, 1625.

(49) Morin, S. A.; Forticaux, A.; Bierman, M. J.; Jin, S. *Nano Lett.* **2011**, *11*, 4449.

(50) Dugue, J.; Adolphe, C.; Khodadad, P. *Acta Crystallogr., Sect. B: Struct. Crystallogr. Cryst. Chem.* **1970**, *B 26*, 1627.

(51) Aitken, J. A.; Cowen, J. A.; Kanatzidis, M. G. *Chem. Mater.* **1998**, *10*, 3928.

(52) Hens, Z.; Moreels, I. *J. Mater. Chem.* **2012**, *22*, 10406.

(53) Moreels, I.; Lambert, K.; Smeets, D.; De Muynck, D.; Nollet, T.; Martins, J. C.; Vanhaecke, F.; Vantomme, A.; Delerue, C.; Allan, G.; Hens, Z. *ACS Nano* **2009**, *3*, 3023.

(54) Leatherdale, C. A.; Woo, W. K.; Mikulec, F. V.; Bawendi, M. G. *J. Phys. Chem. B* **2002**, *106*, 7619.

(55) Yue, W.; Han, S.; Peng, R.; Shen, W.; Geng, H.; Wu, F.; Tao, S.; Wang, M. *J. Mater. Chem.* **2010**, *20*, 7570.